RSC Advances

PAPER

View Article Online
View Journal | View Issue



Cite this: *RSC Adv.*, 2023, **13**, 6779

# Efficient photo-Fenton catalysis using magnetic iron nanoparticles decorated boron nitride quantum dots: theoretical and experimental investigations†

Shinwar A. Idrees,[a] Lazgin A. Jamil*[a] and Khalid M. Omer *[b]

To achieve the efficient removal of pharmaceutical wastes, novel photo-Fenton catalysts, iron-decorated boron nitride quantum dots (**Fe@BNQDs**) were prepared. **Fe@BNQDs** were characterized using XRD, SEM-EDX, FTIR, and UV-Vis spectrophotometry. The decoration of Fe on the surface of **BNQDs** enhanced the catalytic efficiency due to the photo-Fenton process. Photo-Fenton catalytic degradation of folic acid was investigated under UV and visible light. The influence of $H_2O_2$, catalyst dose, and temperature on the degradation yield of folic acid was investigated using Response Surface Methodology. Moreover, the efficiency of the photocatalysts and kinetics was investigated. Radical trapping experiments revealed that holes were the main dominant species in the photo-Fenton degradation mechanism and **BNQDs** played active roles because of their hole extraction ability. Additionally, active species such as $e^-$ and $O_2^{-\bullet}$ have a medium effect. The computational simulation was utilized to provide insights into this fundamental process, and for this purpose, electronic and optical properties were calculated.

Received 12th January 2023
Accepted 13th February 2023

DOI: 10.1039/d3ra00234a

rsc.li/rsc-advances



## 1. Introduction

The worldwide industrial revolution in the 21st century brought a wide spectrum of problems, mainly the contamination of water with harmful and waste materials, leading to significant adverse effects on the environment and wildlife.[1] Water is the common solvent that is available in enough quantity for industrial operations. In most pharmaceutical manufacturing, water is in contact with drugs either as a solvent, product, and/or for cleaning purposes.[2] The contaminated water comes into contact with a river stream or underground water or remains on the surface and then evaporates, leaving chemicals including drugs that bind to sand particles, which again due to erosion by rainwater re-contact with the water body.[3,4]

In recent decades, the removal of harmful chemicals is the research interest in academia and industry. Efforts are being made to develop novel new materials and technologies to remove contaminants, including physical, chemical, and biological wastewater treatments.[2]

Regarding photocatalytic mineralization, most researchers try to achieve a higher rate and more efficient photocatalysts. Heterogeneous photocatalysis uses semiconductor oxides irradiated with UV, near-UV, or visible light at ambient temperature and pressure and in the presence of oxygen.[1,5–8] Nano-sized photocatalysts, specifically the zero-dimensional (0D) nanoparticles, exhibit enhanced photocatalysis efficiency compared to their bulk equivalents. This is caused by the presence of more active sites on the surface, enhanced electron–hole separation, a lower recombination rate, and broad absorption in the visible spectrum, which makes the photocatalyst harvest more energy.[9,10]

Advanced oxidation processes (AOPs) are a group of methods that can produce oxidants with the use of catalysts, potent oxidants, light, or thermal input. They are promising and strong methods for degrading many organic compounds because they produce strong oxidizing agents.[2,3]

The Fenton process in AOPs is regarded as one of the most efficient methods for degrading a wide variety of organic compounds at ambient temperature.[4,11–14] The Fenton process involves the reaction between $H_2O_2$ and ferrous ions in an acidic aqueous solution, leading to the production of hydroxyl radicals ($^{\bullet}OH$).[13] Although the reagents used in the Fenton process are relatively safe to handle and easy to store, however, there are some disadvantages of the Fenton reaction, such as the limited pH range (acidic pHs) and the difficulty of regeneration of the catalyst. Ferrous ions must be added to the reaction medium continuously to sustain the reaction.

To overcome the limitation of the Fenton process, light irradiation was introduced into the Fenton system to form the

[a]*Department of Chemistry, Faculty of Science, University of Zakho, Kurdistan Region, Iraq*

[b]*Department of Chemistry, College of Science, University of Sulaimani, Kurdistan Region, Iraq. E-mail: khalid.omer@univsul.edu.iq*

† Electronic supplementary information (ESI) available. See DOI: https://doi.org/10.1039/d3ra00234a

so-called photo-Fenton process. During the photo-Fenton process, only small amounts of $H_2O_2$ and iron salt are required.[4,11–14] However, more $^{\bullet}OH$ is produced than by the Fenton process or non-Fenton photo processes,[13] which accelerate the degradation rates of a variety of pollutants.

Heterogeneous photocatalysis is a good candidate to harvest light and trigger the Fenton reaction within wider pH ranges.[11,15] Numerous heterogeneous photocatalysts, including metallic nanoparticles,[16–18] metal oxides,[8,19,20] CdS[21–23] and carbon-based nanomaterials[24,25] have been developed.

Boron nitride quantum dots (**BNQDs**) are a class of highly fluorescent quantum dots (QDs).[26–28] It has a wide band gap of 4.5 eV to 6.0 eV, which is not suitable for visible light applications.[29–31] To be utilized for solar-light applications, a narrowing of the band gap is attempted. Angizi *et al.* studied that functionalized boron nitride has an $E_g$ below 4.5 eV, and this might depend on the functional groups of **BNQDs**. Hydroxyl-functionalized **BNQDs** gave $E_g$ 2.3–3.6 eV, methyl functionalized was 3.2–4.2 eV, and amine-functionalized was 3.1–4.0 eV. Thus, the functionalization of **BNQDs** make them a potential tool in photocatalysis research.[32]

In the present work, nanostructured **Fe@BNQDs** were prepared and used to remove folic acid *via* photo-Fenton degradation. A heterogeneous photo-Fenton-like process was applied for this purpose due to the addition of $H_2O_2$ and the presence of Fe nanoparticles on **BNQDs**. Trapping experiments of the reactive species (ROS) were performed to find the active species responsible for the degradation of folic acid. Fig. 1 shows a scheme for the preparation and application of **Fe@BNQDs**.

## 2. Experimental section

### 2.1. Instrumentation

The surface morphological, chemical composition, crystal quality, and structural properties of the synthesized **Fe@BNQDs** were characterized and studied utilizing field-emission scanning electron microscopy (FE-SEM) (SEM 4500-Quanta FEI, USA); the chemical composition of the synthesized nanostructures was measured by energy-dispersive X-ray spectroscopy (EDX) performed in FE-SEM, X-ray powder diffraction (XRD) was used to measure crystal structure using X'Pert PRO (PANalytical, Netherlands) using Kα for copper element (Cu Kα = 1.5406 Å at 40 kV, 30 mA) in the $2\theta$ range of (20° to 70°) and the rate of scanning was 1° $min^{-1}$, respectively. FTIR spectra were recorded using (Thermo Scientific, USA). For monitoring the photodegradation process, absorbance spectra were recorded on a Lambda 25 PerkinElmer UV-Vis spectrophotometer (PerkinElmer, USA).

### 2.2. Chemicals

All chemicals used were of analytical grade and used as purchased without further treatment. Boric acid, iron(III) nitride, sodium oxalate, potassium bromate, and hydrogen

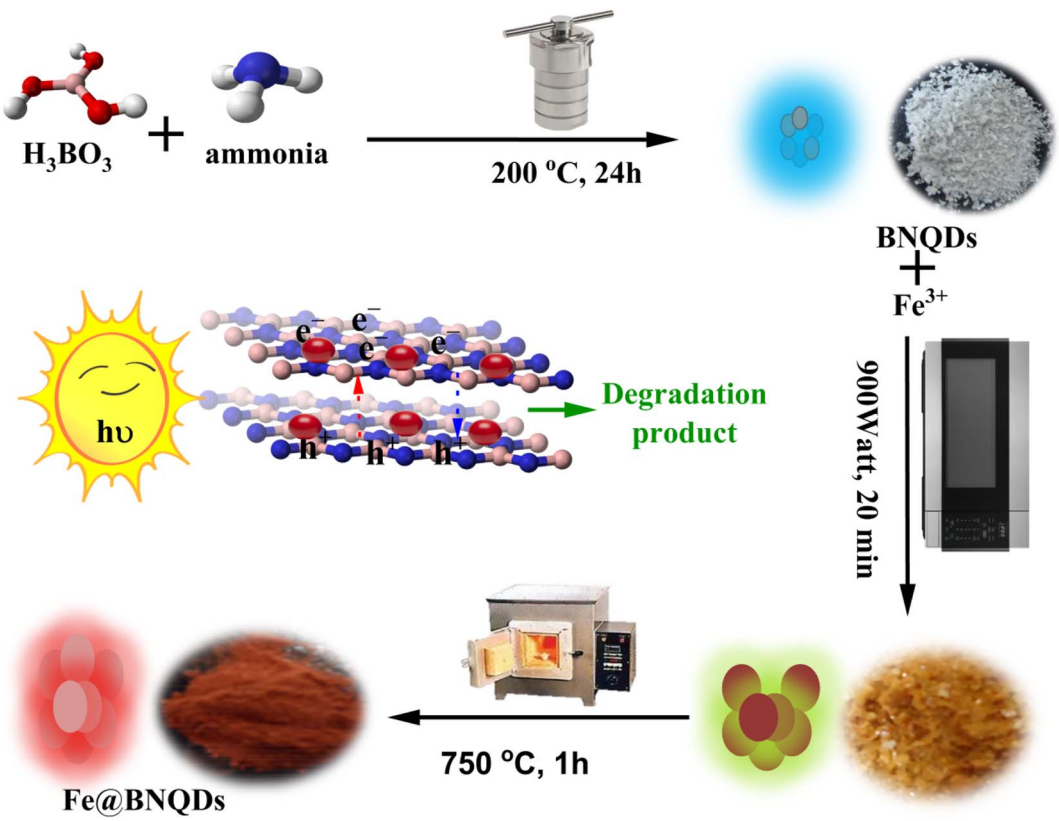


Fig. 1 A schematic diagram demonstrates the preparation and application of Fe@BNQDs.

peroxide were obtained from CARL ROTH GmbH (Karlsruhe, Germany). Ammonia at 25% was purchased from Merck (Darmstadt, Germany). Isopropyl alcohol was purchased from Fluka AG in Sigma Aldrich (Steinheim, Germany). Ascorbic acid was purchased from Scharlau Chemicals (Barcelona, Spain) and folic acid was purchased from UNI-CHEM (China) chemicals.

### 2.3. Synthesis of iron-decorated boron nitride quantum dots (Fe@BNQDs)

First, boron nitride quantum dots (**BNQDs**) were prepared using the hydrothermal method.[33] For every 0.3 g boric acid, 10 mL ammonia 25% was added. The mixture was mixed on a magnetic stirrer for half an hour, then the solution was placed in a Teflon-lined autoclave and heated in an oven for 24 hours at 200 °C. The resulting solution was clear and gave fluorescence with blue-green emission under the UVA light. The solvent was then evaporated, yielding white powder. After this step, for each gram of **BNQDs**, 2.02 mL of 0.1 M $Fe(NO_3)_3 \cdot 9H_2O$ was added with continuous stirring, and then the solution was placed in a microwave oven at 900 W for 20 minutes. The resulting particles were put in a muffle furnace at 750 °C for roughly one hour, Fig. 1 shows the steps in the synthesis of **Fe@BNQDs**. Finally, the powder was purified, washed several times with deionized water, dried, and used in photodegradation applications.

### 2.4. Computational study

The *ab initio* calculations were performed on a plane-wave basis using DFT's pseudopotential methods. All computations were performed using the CASTEP and Dmol$^3$ codes in Material Studio version 2017. We applied non-local-functional generalized gradient approximation (GGA) meta-GGA[34] and hybrid functional including (Becke-3 Parameter-Lee–Yang–Parr) B3LYP[35] and (Heyd–Scuseria–Ernzerhof) exchange–correlation functional HSE06.

Each exchange–correlation (XC) functional was computed using a kinetic energy cut-off: 500 eV at norm-conserving pseudopotentials. The Brillouin zone integration was performed using a $4 \times 4 \times 4$ *k*-point Monkhorst–Pack grid and the self-consistent field (SCF) tolerance was $2 \times 10^{-6}$ (eV per atom). The calculated lattice parameter and band gap values in (eV) are shown in Tables S2 and S3,† respectively. Fig. 6A and B show the band structure and the total density of state for the **Fe@BNQDs** photocatalysts. Hybrid functional B3LYP offered better results and was consistent with the observed data, giving the $E_g$ of about 1.839 eV and 2.295 eV as direct and indirect band gaps, respectively. In addition, this method was used to analyze the band structures and densities of states.

For the band edge study in the vacuum, we did not use the frozen core approximation, the full simulation was carried out with the Fe@BNQD (100) slab model with a lattice parameter of: $a = b = 3.8$ Å and $c = 17.98$ Å in order to avoid the effect of interaction between layers, including 8 atoms. The calculation was carried out using the Dmol$^3$ code for the work function calculation, The (GGA) was applied to treat correlation effects and electron exchange in the (PBE) formulation, and the basis set was determined as the double-numerical plus polarization (DNP) for this job. To improve the results, a 0.005 Ha Fermi-smearing with a 4.6 real space cutoff was used. For the geometry optimization, and work function, respectively, convergence tolerance of 10–5 Ha, 0.002 Ha, and 0.005 was used. The *k*-points were set at $4 \times 4 \times 1$. The optical properties of **Fe@BNQDs** can be illustrated from the complex dielectric function, $\varepsilon(\omega) = \varepsilon_1(\omega) + i\varepsilon_2(\omega)$, which is related to the interaction between photons and electrons. The momentum matrix elements between the occupied levels in the VBM and the vacant levels in the CBM were utilized to calculate the imaginary part $2(\omega)$. The Kramer–Kronig equation can then be applied to derive the real part $1(\omega)$ of the dielectric function from $2(\omega)$. All others, including the electron energy-loss spectrum, optical conductivity, extinction coefficient, and reflectivity, can be determined from $1(\omega)$ and $2(\omega)$.

### 2.5. Photo-Fenton activity

The photocatalytic activity of **Fe@BNQDs** was evaluated through the degradation of folic acid under 5 W of the blue LED (Light Bulb LED GU10 5W 400Lm Grow, GREENICE Co., Madrid, Spain). An ultraviolet water sterilization lamp 220–240 V 50/6 Hz (UVCD215 TS 6 W) was used as a source of UV irradiation. Prior to illumination, according to Table 1, **Fe@BNQDs** along with $H_2O_2$ were dispersed into 25 mL of the solution containing the test compound, and then magnetically stirred in the dark for 60 min to establish an adsorption–desorption equilibrium. At predetermined intervals, 3 mL of the suspension was taken and centrifuged at 8000 rpm for 6 min to remove **Fe@BNQDs**. Then, the absorbance spectra of the folic acid in the supernatants were analyzed using a UV-Vis spectrophotometer at 282 nm. The initial concentration was kept constant at 15 ppm.

To determine the ROS, isopropyl alcohol (IPA) was used as the $^{\bullet}OH$ (hydroxyl radical) scavenger, ascorbic acid as $^{\bullet}O_2^-$ (superoxide radical) trapping species, sodium oxalate and potassium bromate were added as scavengers for $h^+$ and $e^-$, respectively.[28,36–39]

## 3. Result and discussion

### 3.1. Characterizations of Fe@BNQDs

The FTIR spectra were used to investigate the formation of **BNQDs** and then the formation of **Fe@BNQDs**. Fig. 2A shows the FTIR spectra of **BNQDs** and **Fe@BNQDs**, respectively. The

Table 1 Levels of the parameters studied in BBD statistical experiments

| | | Levels | | |
|---|---|---|---|---|
| Independent variable | Unit | −1 (low) | 0 (middle) | +1 (high) |
| **Fe@BNQDs** | g/100 mL $H_2O$ | 0 | 0.05 | 0.1 |
| $H_2O_2$ | M | 0 | 0.2 | 0.4 |
| Temperature | °C | 20 | 30 | 40 |

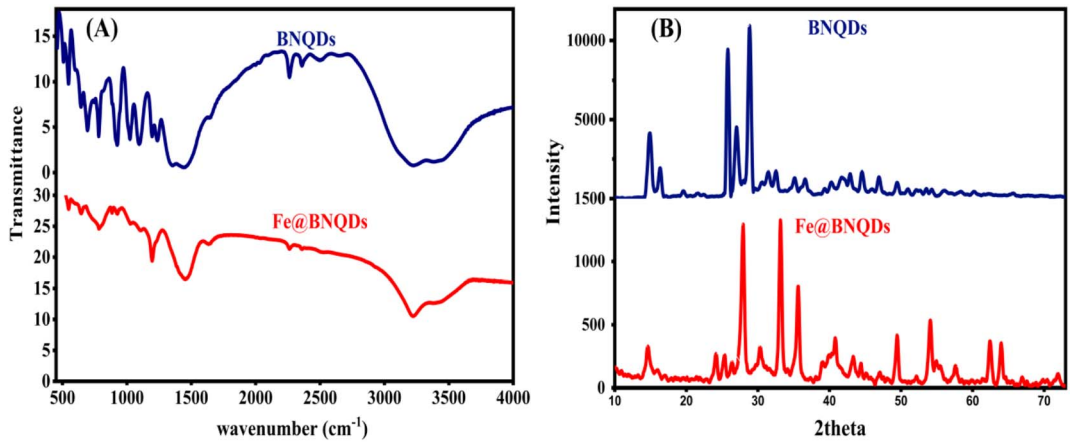


Fig. 2 XRD and FTIR pattern of the fabricated **Fe@BNQDs**: (A) FTIR of **BNQDs** and **Fe@BNQDs**, (B) XRD of **BNQDs** and **Fe@BNQDs**.

peaks at 457.86 $cm^{-1}$, 506.33 $cm^{-1}$, and 545.75 $cm^{-1}$ are assigned for **BNQDs**.[40] The peaks at 642.35 $cm^{-1}$ and 693.19 $cm^{-1}$, are assigned to B–O bond vibrations.[41,42] Another peak was observed at 781.11 $cm^{-1}$ due to the amorphous nature of **BNQDs** and the B–N–B bending mode.[40,43–46] The peak at 924.75 $cm^{-1}$ is for the B–N–O vibration mode.[40,47] The peaks at 1022.77 $cm^{-1}$, 1093.4 $cm^{-1}$, 1194.87 $cm^{-1}$, and 1234.03 are similar to the related results of **BNQDs** elsewhere.[40,44–46,48] Moreover, two peaks at 2261.93 $cm^{-1}$ and 2358.83 $cm^{-1}$ resulted from the bending vibration of B–H. The presence of oxygen functional groups is clear from the FTIR spectra of both **BNQDs** and **Fe@BNQDs**. The broad peak at 1450 $cm^{-1}$ is due to the bending mode of B–OH[41] and the stretching mode of B–N.[42] In addition, a peak at 2498.22 $cm^{-1}$ and a broad peak at 3207.55 $cm^{-1}$ have resulted from the stretching vibration mode of B–OH and B–$NH_2$.[44,46,49]

Compared with the FTIR spectrum of **Fe@BNQDs**, there were some additional signals after **BNQDs** were decorated with Fe atoms; the bands at 547.09 $cm^{-1}$ have resulted from the Fe–N stretching mode,[50] and 642.8 $cm^{-1}$ is ascribed to the Fe–O stretching vibration mode,[51–53] the bands at 1633.46 $cm^{-1}$ and 3220.28 $cm^{-1}$ correspond to Fe–OH bending and stretching vibration, respectively.[52–54]

The crystal structure of the product was analyzed using powder XRD spectra. Fig. 2B shows the XRD pattern of **BNQDs**; the diffraction peaks of 2$\theta$ (theta) equal to 14.77°, 16.12°, 25.12°, 26.27°, 30.52°, 31.52°, 34.02°, 35.42°, 38.02°, 38.92°, 40.37°, 40.72°, 41.37°, 42.97° can be indexed to the corresponding crystal planes 111, 020, 202, 122, 222, 113, 213, 322, 313, 422, 242 that match from the JCPDS card (no. 40-65-373).[55] Another peak at 28.02° is related to the face 002.[56]

Fig. 2B displays the XRD pattern of **Fe@BNQDs**, the peaks are located at 2$\theta$ (theta) equal to 14.62° (boron nitride, BN, and $Fe_3B$),[57] 24.15° ($Fe_2B$),[58] 26.4° (BN), 27.93° (BN $Fe_2B$),[58] 33.1° ($Fe_3B$),[57] 35.62° ($Fe_2B$),[58] 40.83° (BN and $FeN_{0.06}$),[59] 43.35° (BN, $Fe_2N$),[60] 44.4° (BN) 49.48° ($Fe_2B$),[58] 54.1° ($Fe_3B$),[57] 54.93° (BN), 55.48° (BN), 57.62° ($Fe_3B$),[57] 62.45° ($Fe_2N$),[60] 64° ($Fe_2N$),[60] 71.93° (BN, $Fe_2N$),[60] these data match with those obtained from the JCPDS cards (no. 96-101-1241,[61] no. 96-201-6174,[62] no. 96-101-0603,[63] and 96-101-0332 (ref. 64)). The other two peaks, 25.35° (BN) and 30.33° (BN and $Fe_2N$)[60] are found in other ref. 65 and 66.

An XRD pattern was used to measure the crystallinity index (CI),[28,67,68] which was found to be 68.8 for **BNQDs** before decoration with Fe and 76.6 for **Fe@BNQDs.** It is worth mentioning that CI was measured from the ratio of the integrated area of all crystalline peaks to the total integrated area under the XRD peaks. The FTIR spectra were characterized to investigate the formation of **BNQDs** and then the formation of **Fe@BNQDs**.

The detection of oxygen, iron, nitrogen, and boron is shown in Fig. 3B, which corresponds to the EDX spectra of the **Fe@BNQDs** sample. It is worth mentioning that the presence of oxygen is due to the hydroxyl functionalized on the surface, which makes nanoparticles soluble in water.[69,70] However, the high content of oxygen that appeared in the EDX map (Fig. 3B) is due to the hydrophilic nature of **BNQDs**, which is due to the functionalized hydroxyl groups on its edge.[26,27,32,71] Fig. 3A shows the morphology of **Fe@BNQDs** as imaged by SEM. It can be clearly seen that sphere-like nanostructures were prepared with sizes between 60 and 65 nm. In addition, the Scherrer equation and the Williamson-Hall (W–H) equation were applied to measure the average particle size, and it was found that the average particle size of **Fe@BNQDs** was about 26 nm according to the Scherrer equation and 31 nm according to the W–H equation.

### 3.2. Photocatalytic degradation

**Fe@BNQDs** were prepared and subjected to the heterogeneous photo-Fenton process. To study the effects of $H_2O_2$, **Fe@BNQDs**, and temperature, the design of the experiment (DOE) and statistical analysis were performed. All the operational variables and their levels applied for designing the experiment are summarized in Tables 1 and 2.

Response surface methodology (RSM) is a statistical analysis method that utilizes the experimentally obtained quantitative data and, from the design of the experiment and based on practical data, develops the regression equation, which is beneficial for the optimization and prediction of the effect of operating parameters and conditions in the photo-Fenton degradation process.[72,73]

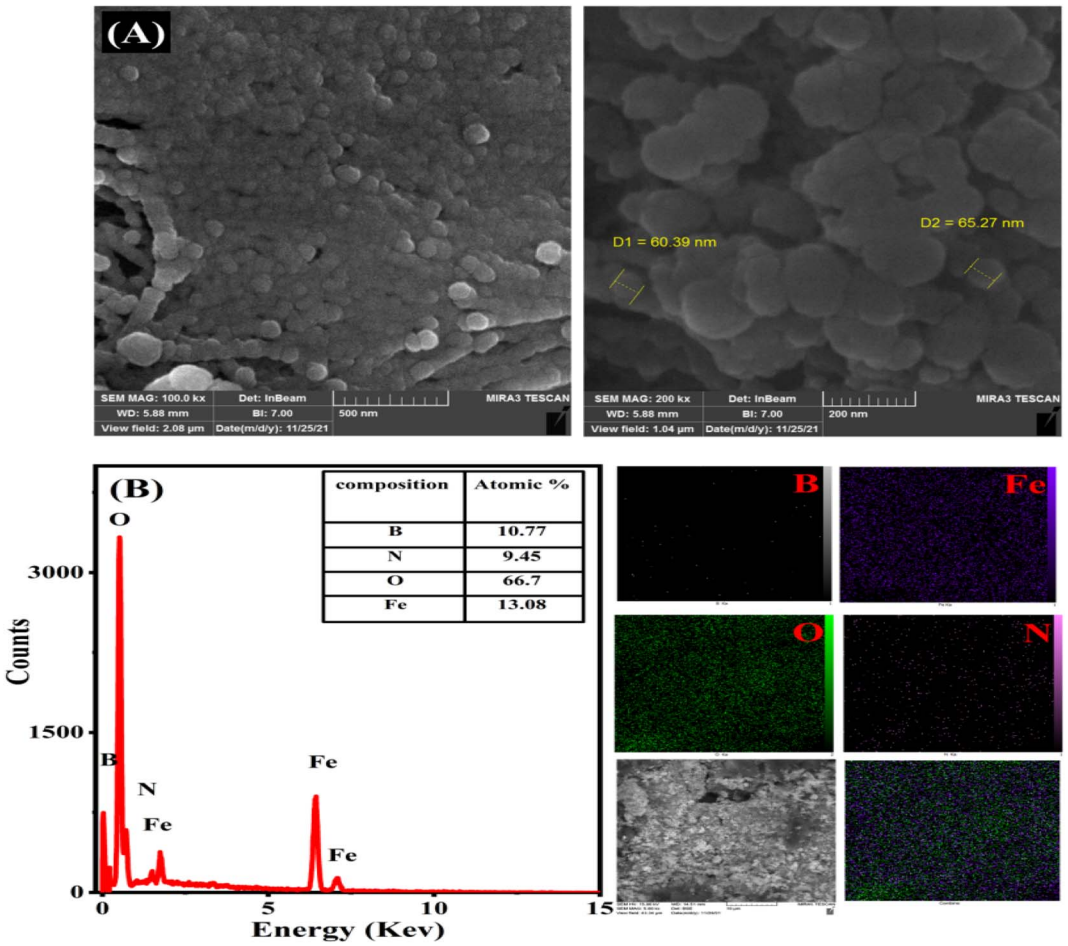


Fig. 3 (A) SEM images of **Fe@BNQDs** and (B) EDX spectrum and total map of the elemental ratio of **Fe@BNQDs**.

Table 2 Central composite design matrix Box–Behnken design BBD with fitted and observed values[a]

| Run order | **Fe@BNQDs** (g/100 mL) | $H_2O_2$ (M) | Temp. (°C) | % of degradation, observed | % of degradation, fitted |
|---|---|---|---|---|---|
| 1 | 0 | 0 | 30 | 0 | −1.684 |
| 2 | 0.1 | 0 | 30 | 1.77 | 1.143 |
| 3 | 0 | 0.4 | 30 | 0 | 0.344 |
| 4 | 0.1 | 0.4 | 30 | 6.38 | 7.781 |
| 5 | 0 | 0.2 | 30 | 0 | 1.278 |
| 6 | 0.1 | 0.2 | 20 | 9.58 | 9.235 |
| 7 | 0 | 0.2 | 40 | 0 | 0.062 |
| 8 | 0.1 | 0.2 | 40 | 3.93 | 2.369 |
| 9 | 0.05 | 0 | 20 | 0.7 | 1.248 |
| 10 | 0.05 | 0.4 | 20 | 12.2 | 10.719 |
| 11 | 0.05 | 0 | 40 | 0.58 | 2.344 |
| 12 | 0.05 | 0.4 | 40 | 1.805 | 1.540 |
| 13 | 0.05 | 0.2 | 30 | 6.12 | 5.162 |
| 14 | 0.05 | 0.2 | 30 | 4.72 | 5.162 |
| 15 | 0.05 | 0.2 | 30 | 5.2126 | 5.162 |
| 16 | 0.1 | 0.2 | 30 | 4.6 | 5.732 |

[a] pH was kept constant at 7, and 1 hour photodegradation all **Fe@BNQDs** samples were adsorption–desorption equilibrated for one hour in the dark, and the light source was blue LED light 5 × 1 W.

The study was applied by utilizing the widely used Box–Behnken design (BBD). The main advantage of the BBD study is that it reduces the total number of experiments required to determine the photocatalysis degradation yield.[4,73–75] The BBD was performed for three independent variables, including $H_2O_2$ concentration, **Fe@BNQDs** dose, and temperature. The

observed dependent variable was the degradation percentage of folic acid. Three levels were determined for each independent variable, as shown in Table 1. A total of 16 runs were assigned and then analyzed.

The results of the ANOVA for photodegradation efficiency and the RSM model fitting of folic acid removal using **Fe@BNQDs** are presented in Table S1.† The ANOVA analyses were based on the F-test method and *p*-values. For data manipulation, the proposed parameter was deemed significant at a 95% confidence interval.[74,75] The lack of fit (LOF) is another parameter used to determine the validity of the model, which exhibits and determines the random error in the achieved data. LOF is supposed to be not significant in a reliable model; here, LOF has a value of 8.21 as an F-test and 0.111 as a *p*-value, which is not significant, so the model is reliable.

From the ANOVA results shown in Table S1,† it can be concluded that the overall regression is significant with a *p*-value of 0.027. Regarding the regression equation with linear, square, and interaction terms for all selected parameters, the results show that **Fe@BNQDs** dose and $H_2O_2$ are affecting the percentage of degradation linearly with *p*-values of 0.026 and 0.014, respectively, but there is no significant effect when the parameter values are squared. In addition, the interaction between the peroxide concentration and temperature gives a significant result with a *p*-value of 0.024. It can lead to the conclusion that the terms are affecting the degradation yield linearly.

The regression coefficients were determined, and the results were analyzed using Minitab software version 17. The quality of the fit for the model was expressed from the *p*-value and correlation coefficient ($R^2$) of 91.41%. The calculated coefficient from the quadratic regression equation is shown in Table S1.† The magnitude and sign of the coefficients represent the influence of each parameter over the response. According to the coefficient presented from the quadratic regression model, the term with the highest coefficient is for the **Fe@BNQDs** dose with a value of 192.879, which means it is a dominant factor in the overall responses. The positive value of the coefficient means a synergetic effect; however, the negative value of the coefficient means an antagonistic effect. Specifically, the interaction term of temperature and $H_2O_2$ concentration by a factor of −1.284 shows the most antagonistic effect on the degradation of **Fe@BNQDs**, which have a significant *p*-value of 0.024.

The observed degradation percentage of folic acid varied between zero degradation in the absence of a photocatalyst and 12.2% in the presence of a photocatalyst after one-hour irradiation by a LED-5 W visible lamp, and the model prediction was matched with the experimental results satisfactorily. Control experiments were performed using Fe ions alone along with peroxide and without **BNQDs** and the result was zero degradation, **BNQDs** as photocatalysts were also tested and they were not active under visible light; in addition, another experiment for **Fe@BNQDs** was carried out in the dark, and the result showed no degradation. Thus, we can conclude from these experiments that **Fe@BNQDs** are responsible for and are involved in photo-Fenton degradation.

**3.2.1 Kinetic study and efficiency of photocatalysis.** To study the kinetics of photodegradation, first, the best experiment was selected, which is run number 10 in Table 2. The experiment was conducted under the same conditions and radiation source. The rate of folic acid degradation was estimated by examining the degradation at 282 nm. To determine the order of degradation, the log–log graphical method, and the integral and deferential rate laws were applied. The goodness of the kinetic order can also be evaluated by the correlation coefficient ($R^2$) when the value of $R^2$ is close to unity.[3,4,8,76] It appears that the degradation at peak 282 nm is the first order with an $R^2$ value of 0.998 compared to the second order, which is 0.97, as shown in Fig. 4A and B, the same procedure was repeated when irradiating with UV light, as shown in Fig. 4C and D, respectively. The result shows that the degradation percentage after one hour of irradiation was tripled in the case of 35% degradation with UV light. As regards the rate constant, degradation that occurred under irradiation with UV light was 12.77 folds faster than that with visible light, with rate constants equal to $6.4 \times 10^{-4}$ $min^{-1}$ and 0.0082 $min^{-1}$ for visible light and ultraviolet, respectively.

With respect to the degradation efficiency, the sample was irradiated for 24 hours each time. From Fig. S1,† it can be concluded that the efficiency was 77.1% after 24 hours of irradiation of folic acid with **Fe@BNQDs** using 5 W of blue LED light. The efficiency dropped to 58.5% for the next 24 hours, and then to 36.36% for the next 24 hours. The photocatalyst was then dried and activated at 150 °C for two hours and then used in photodegradation for the next 24 hours. The efficiency was found to increase to 58.61%.

**3.2.2 Effect of initial pH on photocatalysis.** The photocatalytic degradation of folic acid over **Fe@BNQDs** at five different pHs was studied. Fig. 5C illustrates the effect of different initial pHs on the photocatalytic efficiency. The results showed that the pH of the solution had a great influence on the photodegradation of folic acid over **Fe@BNQDs**. In general, as the pH of the solution increases, the degradation efficiency decreases, and the best degradation yield was at an acidic medium pH = 3, where 24.5% was removed, and at a very basic solution pH = 11, the photocatalyst was inactive. As a general rule, the electrostatic effect influences the adsorption and desorption between the surface of the photocatalyst and target molecules; therefore, an oppositely charged photocatalyst and pollutants cause attraction. Accordingly, the point of zero charge, $pH_{PZC}$ (isoelectric point pH) plays an important role in determining the critical value and magnitude of the charge held between the photocatalyst and pollutants during the photocatalytic processes,[11,77,78] the oxide-containing photocatalysts are amphoteric in nature, and they turn to an acidic or basic surface as in the following eqn (1) and (2):

$$\text{Photocatalyst–OH} + H^+ \rightarrow \text{photocatalyst–}OH_2^+,\ pH < pH_{PZC} \quad (1)$$

$$\text{Photocatalyst–OH} + OH^- \rightarrow \text{photocatalyst–}O^- + H_2O,\ pH > pH_{PZC} \quad (2)$$

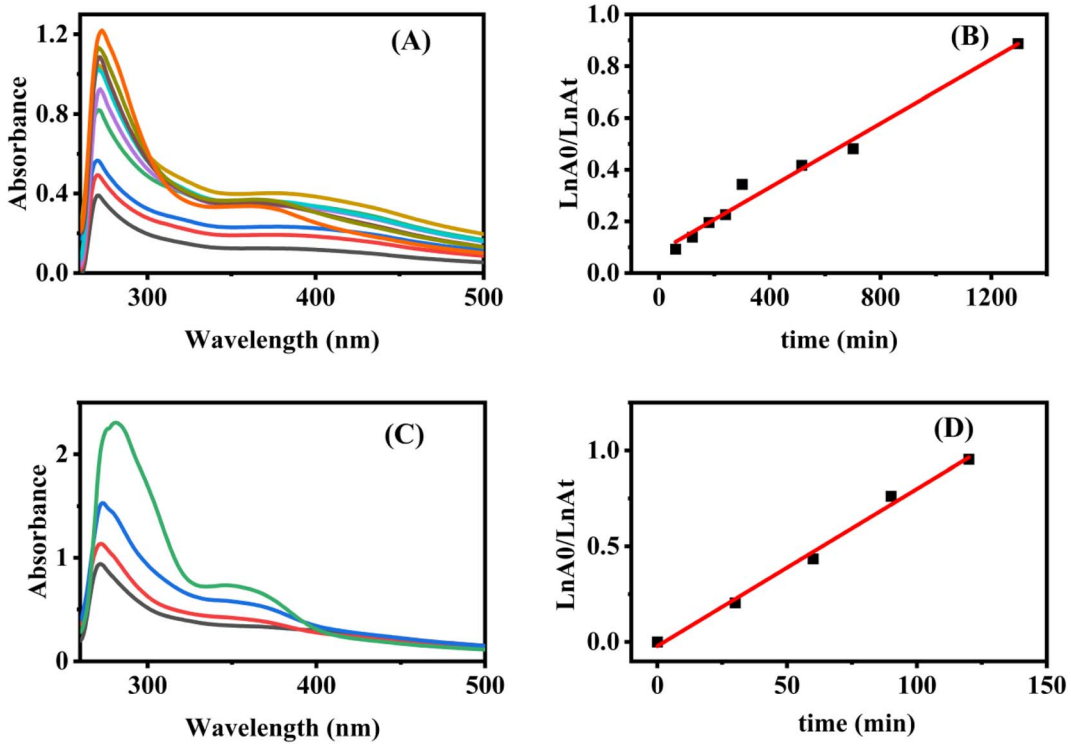


Fig. 4 The change in UV-Vis spectra as a function of time of 15 ppm folic acid by (A) visible light, (C) ultraviolet light. The integral kinetic plot of (B) 1st order visible light and (D) 1st order ultraviolet light at 25 °C.

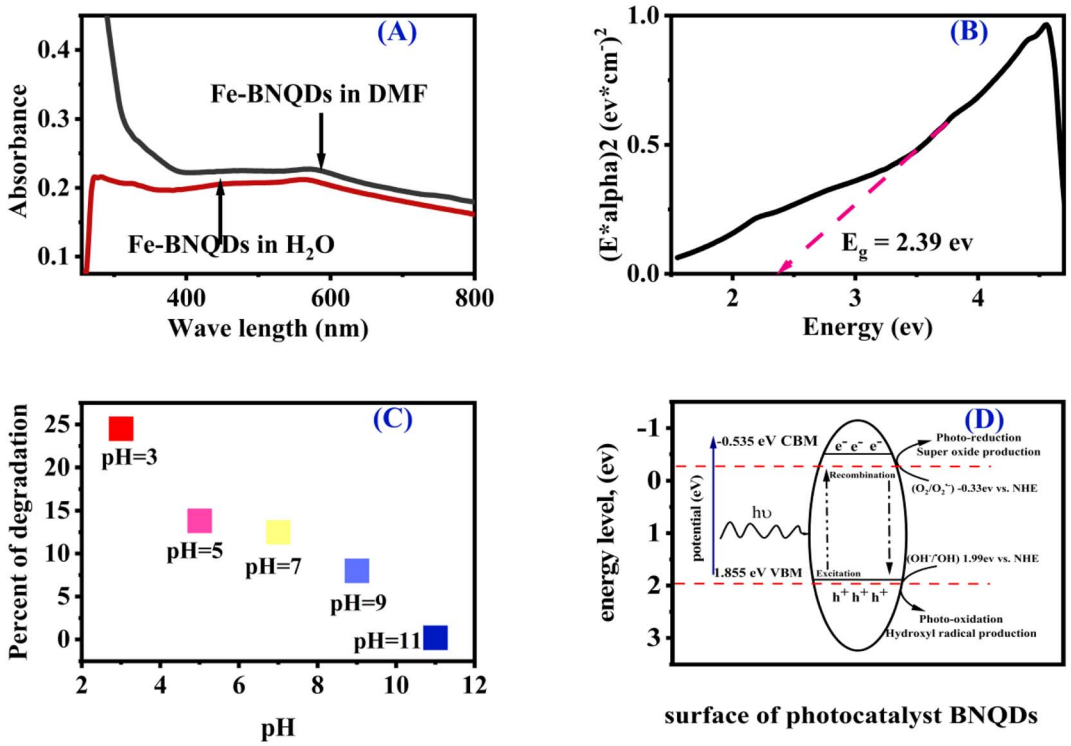


Fig. 5 (A) UV-vis. Absorption spectra. (B) Tauc plot (alpha $h\nu)_2$ *versus* energy band gap ($h\nu$) of **Fe@BNQDs**. (C) Effect of initial pH on the photocatalytic degradation of folic acid over **Fe@BNQDs** and (D) Schematic diagram illustrates the principal mechanism of **Fe@BNQDs**.

Based on this information, it could be deduced that the initial pH determines the attraction or repulsion between the surface of the photocatalyst and pollutants. At pH values lower than $pH_{PZC}$, the photocatalyst surface is positively charged, so, it is able to attract negatively charged molecules. At pH equal to $pH_{PZC}$, there is no charge on its surface, while at pH greater than $pH_{PZC}$, the surface of the photocatalyst is negatively charged.[28,77,78] Regarding the folic acid degradation over **Fe@BNQDs**, the acidic medium pH 3 was optimum, it can be concluded that the pH 3 is close to the $pH_{PZC}$ of **Fe@BNQDs**; as a result, the surface is positively charged, which is able to attract the negatively charged folic acid molecule. As has been seen in trapping experiments, which confirms that the $h^+$ plays a major role in the photodegradation process of folic acid over **Fe@BNQDs**.

### 3.3. Photo-Fenton mechanism and scavenger trapping experiments

The progress of the photocatalytic reaction and mineralization of chemical waste was attained by the transfer and transition of active species $h^+$, $e^-$, $^{\bullet}O_2^-$, and $^{\bullet}OH$. Which made it possible to confirm the major active radical species that take part in the photodegradation process and the photocatalyst reaction mechanism. As shown in Fig. S3,† it can be seen that the degradation of folic acid was hardly affected by isopropyl alcohol (IPA), while the degradation percentage declined significantly with the addition of $Na_2C_2O_4$ and decreased in the presence of ascorbic acid and $KBrO_3$. Accordingly, the results indicated that the degradation percentage lowered in the presence of $h^+$, $e^-$, and $^{\bullet}O_2^-$ trapping species, indicating that $h^+$, $e^-$, and $O_2^{-\bullet}$ were responsible for folic acid degradation over **Fe@BNQDs** PC. The addition of IPA to the photocatalytic reaction was not significant, which demonstrates that **Fe@BNQDs** are inert for the production of $OH^-/^{\bullet}OH$ due to the position of the band edges.

Regarding the band structure of the prepared photocatalyst, first UV-visible absorption spectra were recorded both in water and the DMF solvent, as shown in Fig. 5A, then a Tauc plot was plotted, and the results were in good agreement with those from the theoretical DFT calculation.[79,80] The $E_g$ of **Fe@BNQDs** was evaluated from the Tauc plot and it was estimated to be 2.39 eV. From the optical absorption spectra in Fig. 5A, we found that the **Fe@BNQDs** showed optical absorption that extended more into the visible region, which indicates more energy harvesting.

To elucidate the energy level (band edges) of the prepared nanostructured photocatalysts, photo redox potential was calculated, as shown in Fig. 5D. $E_{VB}$ was estimated to be 1.855 eV and $E_{CB}$ −0.535 eV. The potentials of **Fe@BNQDs** were measured using the Mulliken electronegativity rules:[28,37,81–86]

As presented in Fig. 5D, the energy of the valence band maximum $E_{VB}$ of **Fe@BNQDs** was estimated to be 1.855 eV, which is more negative than that of ($OH^-/^{\bullet}OH$) (1.99 eV *versus* NHE); as such, the hole ($h^+$) at VBM is unable to oxidize $OH^-$ to produce the hydroxyl radical ($^{\bullet}OH$); simultaneously, the CBM potential was measured to be −0.535 eV *versus* NHE, which is less positive than that of $O_2/O_2^{\bullet-}$ −0.33 eV *versus* NHE,[22,38] as such, the electron at the CBM band edge can react with $O_2$ to form $O_2^{\bullet-}$; these results are in good agreement with the scavenger test, which strongly indicates that $h^+$ and superoxide $O_2^{\bullet-}$ radical are both the active species involved in the photodegradation of folic acid over **Fe@BNQDs**.

### 3.4. Computational simulation

To gain a better understanding of the prepared nanomaterials, theoretical calculations were performed. The perfect band gap is a direct gap semiconductor of 1.839 eV at the *X* point and an indirect band gap of 2.295 eV at the *M* point at the Valance Band Minimum (VBM) to the G–R at the Conduction Band Maximum (CBM), as shown in Fig. 7A. The band gap of the **Fe@BNQDs** was observed to decrease after decorating with Fe atoms, from 3.79 eV to 2.39 eV for **Fe@BNQDs**. It is obvious from Table S3,† which reports $E_g$ the most XC functionals that exhibit better agreement with the experimental results are B3LYP, therefore, the B3LYP functional was used to interpret, discuss, and analyze the band structure and density of states as it gives correct and sufficient data.

The partial density of state (PDOS) of the electronic levels of **Fe@BNQDs** is plotted in Fig. 6B. It can be noted that the Fermi level is close to VBM. As regard to Fe atoms, the d-orbital showed a high DOS that covers the Fermi level at the valence band, which appears as two broad peaks within the range of (−2.98 to 0.55 eV), which explains that most of the DOS of Fe atoms are located at the 3d-orbital. The bottom of the conduction band consists of mixed 4p and 3d-orbitals with medium intensity at 2.99 eV, Fig. 6B. With respect to boron atoms, they have one broad peak near VBM at −1.83 eV and another peak at −3.94 eV, both belonging to 2p orbitals. Regarding CBM, there are three peaks that belong to 2p-orbitals within the range of (2.34 to 6.48). As for nitrogen atoms, one peak overlaps with the Fermi level at VBM, and one peak is observed at −1.74 eV; at CBM, a peak is observed at 2.82 eV, which belongs to the 2p-orbital with a high DOS and the 2s-orbital with a lower DOS. It can be seen from Fig. 6B that the s-orbitals for Fe, B, and N atoms have a minimum contribution to DOS at VBM and CBM.

As shown in Table S2,† the optimized lattice parameter and bond length for **Fe@BNQDs** and hexagonal boron nitride (h-BN) were computed utilizing PBE exchange functionals.[28,87,88] It is reported that the total volume of the cell increased after the insertion of the Fe atom and that the overall structure changed. That has an effect on the B–N bond length and the shape of the cell.

To investigate the electronic density available on elements in the ground and excited states of **Fe@BNQDs**, first, a single sheet of **Fe@BNQD** 1.5 nm was optimized. The highest occupied molecular orbital (HOMO) and the lowest unoccupied molecular orbital (LUMO) were calculated using the DFT/GGA/PBE $Dmol^3$ code. As illustrated in Fig. 6C, the electron density at the hydroxyl group of **BNQDs** in HOMO (ground state) is concentrated at the Fe atom in LUMO (excited state), implying that the $OH^-$ functional groups at the edges of the **BNQDs** inject electrons to the Fe atom and are thus most are involved in the photocatalysis process.

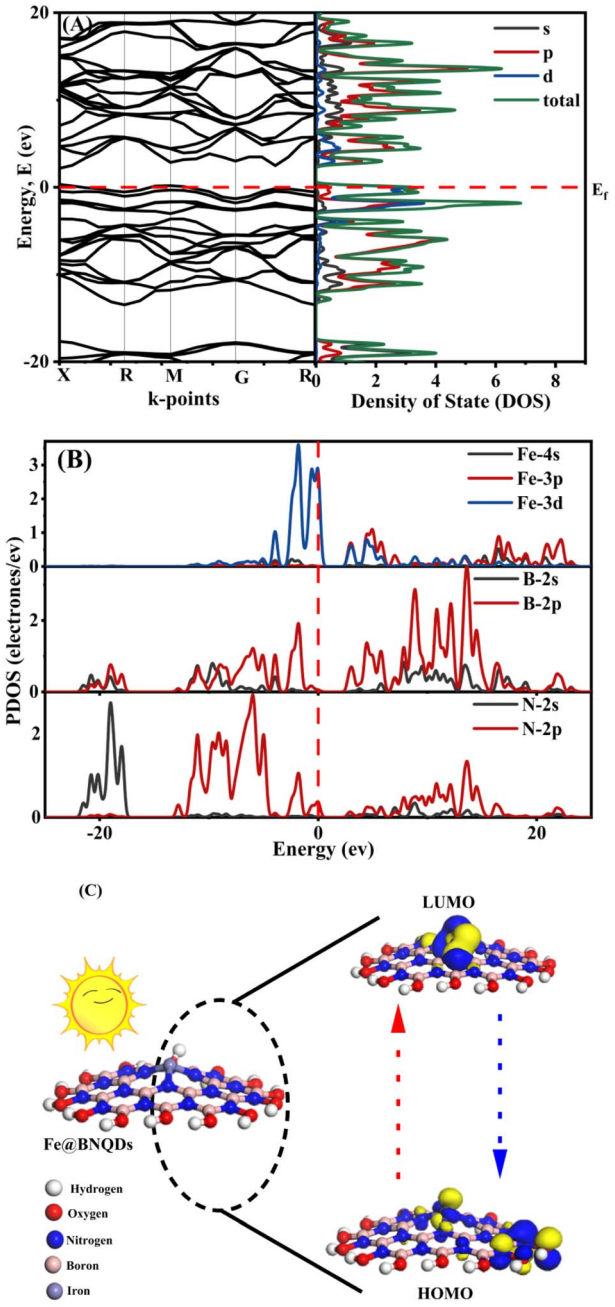


Fig. 6 (A) Band structure and total density of state for pure **Fe@BNQDs** photo-catalyst, (B) The PDOS of the **Fe@BNQDs** utilizing DFT/B3LYP/norm-conserving. (C) Molecular orbital transferee during excitation from HOMO to LUMO by the DFT/GGA/PBE Dmol$^3$ code.

In this study, we characterized the structural stability of the **Fe@BNQDs** photocatalyst at high temperatures using thermodynamic parameters. The standard statistical thermodynamic functions: Gibbs free energy, heat capacity, entropy, and enthalpy for **Fe@BNQDs** were provided from the vibrational harmonic frequencies in the temperature range of 25–1000 K, as shown in Fig. S2.† In general, it can be noticed that these thermodynamic functions are increasing with temperature except for Gibbs free energy;[89–91] Gibbs free energy is negative at 825 K, so that, the formation of **Fe@BNQDs** is only achievable at elevated temperatures. At this point, the value of entropy is 466 cal mol$^{-1}$ K$^{-1}$ and the enthalpy is 379 kcal mol$^{-1}$ K$^{-1}$.

It is well known that one of the crucial characteristics for semiconductors to function as photocatalysts is the position of the valence and conduction band edges. It establishes the photochemical reaction's thermodynamic limit, which is carried out by photogenerated electrons and holes. In general, the conduction band and valence band margins of the photocatalyst should be between the redox potentials of the reactants. The band edges in a vacuum were calculated, as shown in Fig. 7, the band edge calculations illustrated that the **Fe@BNQDs** is an efficient visible-light-driven photocatalyst for the degradation of organic wastes and it may be suitable for water splitting and $CO_2$ reduction as well.

In optoelectronic fields, such as photocatalysis, the optical characteristics of semiconductor materials are of utmost significance since they can explain the behavior of the photocatalyst during photochemical interactions. The spectra of **Fe@BNQDs** as a function of photon energy ranging from 0.01 up to 60 eV are shown in Fig. 8. The extension of electrical transport to large (optical) frequencies is the optical conductivity; this quantitative evaluation is contact-free and mostly responsive to charged responses. Fig. 8A shows the optical conductivity spectra; the maximum optical conductivity regarding the UV visible region is shown at 3.2 eV.

Another important optical characteristic is the electron energy loss function. The energy loss experienced by rapid electrons moving through a substance is described by the loss function. The surface plasmon resonance is linked to the loss function's peaks, Fig. 8B shows the loss function spectra; there are no peaks observed in the UV visible area, therefore, we can say that this photocatalyst has an absent plasmonic effect. The dielectric function plays a significant role in explaining how radiation behaves inside a photocatalyst. The imaginary portion

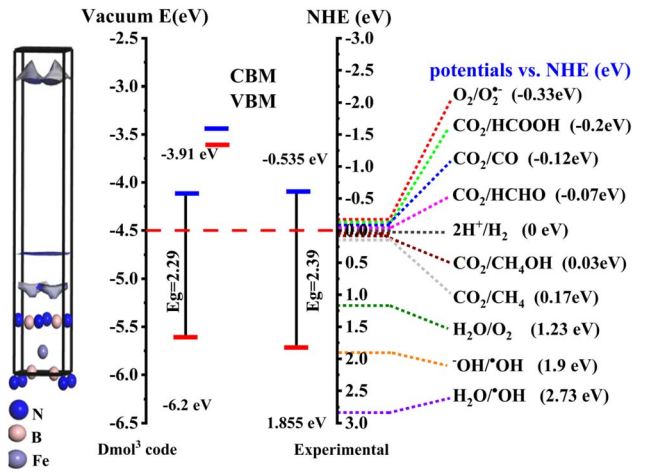


Fig. 7 Bandgaps and band-edge positions with respect to the vacuum level and NHE for the **Fe@BNQDs**. EVB (red bar) and ECB (blue bar) of the **Fe@BNQDs** photocatalyst in vacuum and experimental; along with the potentials of $CO_2$ reduction, water splitting, and photodegradation processes at normal hydrogen electrode (NHE) scale at pH = 0.

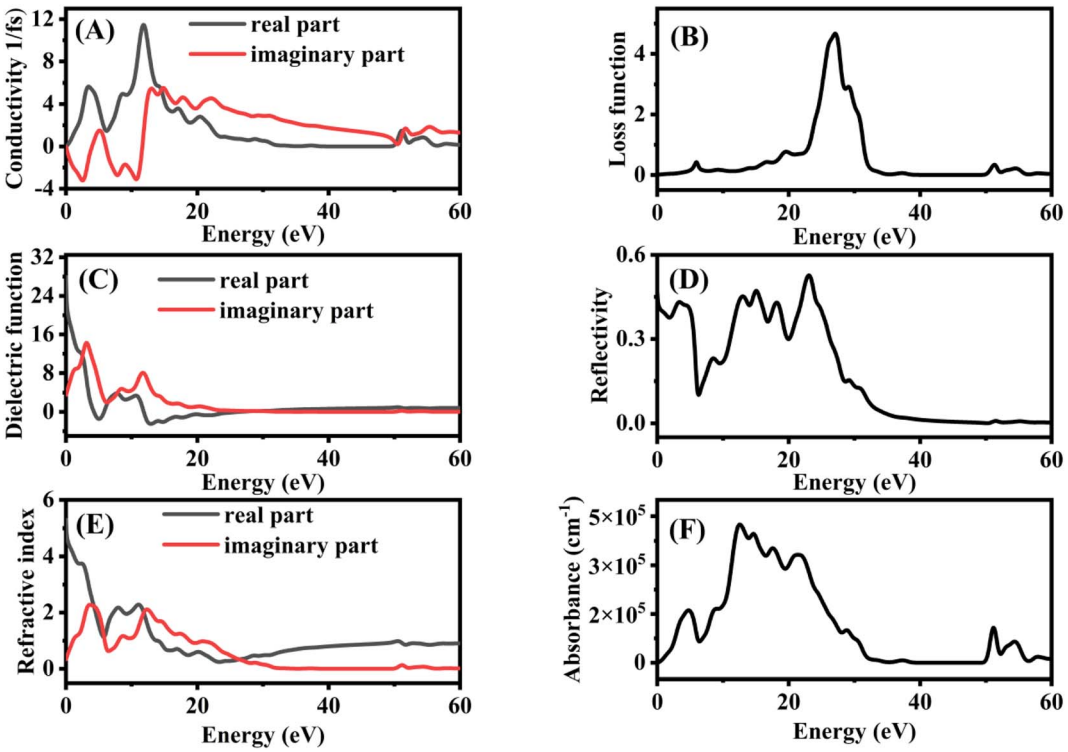


Fig. 8 Optical properties spectra of Fe@BNQDs (A) conductivity, (B) loss function, (C) dielectric function, (D) reflectivity, (E) refractive index, and (F) absorption.

of the dielectric function is related to the band structure and absorption characteristics of the photocatalysts. The dielectric function demonstrates what a passing light beam or other electric fields would do to a photocatalyst. The complex dielectric function's imaginary part $\varepsilon_2(\omega)$ denotes the quantity of absorption in a material, while its real part $\varepsilon_1(\omega)$ denotes the polarization of the photocatalyst caused by the propagating light. Fig. 8C shows the dielectric function spectra, the two major peaks are observed at 3.2 and 11.8 eV. The frequent inter-band transitions between VBM and CB are represented by the imaginary dielectric function, which is a significant quantity. **Fe@BNQDs** have a first peak that is caused by the optical transition according to the band gap value, which is 2.4 eV, followed by two further peaks. The reflectivity spectra, shown in Fig. 8D, exhibit the optical reaction of the systems to the incident light. In terms of reflectivity, a lower energy bandgap results in a higher $\varepsilon_1(0)$ value and hence a higher reflection coefficient, and *vice versa*, the reflectivity of **Fe@BNQDs** is more significant in the infrared to the UV region.

The refractive index explains how interactions with photocatalysts alter light waves (amount of light reflected or bent). The imaginary part, which is called the extension coefficient of the refractive index, indicates the reduction of an electromagnetic wave moving through a photocatalyst, whereas, the real part measures the phase velocity of the electromagnetic wave in a medium. The real and imaginary components of the refractive index are connected by the complex dielectric function; Fig. 8E shows refractive index spectra. **Fe@BNQDs** exhibit a high value of the extension coefficient at the infrared region and a decrease in the visible and UV regions, while the real part has a low value in the infrared, then increases in the visible region and decreases again at the UV region. Reflectivity refers to the ratio of the amount of light that strikes a substance to the amount of light that is reflected from it. By synchronizing the electric and magnetic fields at the surface, it is possible to obtain the reflection coefficient for the basic case of normal incidence onto a plane surface. The absorption coefficient offers useful information when the UV-Vis energy is applied to achieve optimum efficiency, and absorption coefficient spectra are shown in Fig. 8F; in general, **Fe@BNQDs** exhibit good adsorption in the UV visible region, which is of interest in photocatalysis.[88,92–97]

## 4. Conclusions

A novel magnetically-separable and visible-light-driven photo-Fenton catalyst (**Fe@BNQDs**) was synthesized and characterized. **Fe@BNQDs** indicated efficient degradation of folic acid. The RSM based on BBD was employed to demonstrate the degradation efficiency of folic acid under the influence of three variables, including **Fe@BNQDs** dose, $H_2O_2$ concentration, and temperature. According to the ANOVA and regression coefficients, the results showed that the effect of the operating variable is a linear positive *p*-value of 0.013, and the effect of $H_2O_2$ and temperature interaction was a negative *p*-value of 0.024. The photocatalytic efficiency tests revealed that the **Fe@BNQDs** have good stability; the experiment lasted for 96 hours under irradiation. Trapping experiments were performed to

investigate the active species and possible mechanisms involved in photodegradation over **Fe@BNQDs**. Analysis of the results shows that the **Fe@BNQDs** are inert toward the production of the $^{\bullet}OH$ radical, and the active species are $h^+$, $e^-$, and $O_2^{\bullet}$. A theoretical study was performed on the basis of the DFT framework, regarding the electronic structure. The B3LYP/DFT hybrid function gives a better result and is closer to the experimental value.

## Conflicts of interest

The authors declare there are no conflicts to declare.

## References

1 R. C. Pawar and C. S. Lee, *Heterogeneous Nanocomposite-Photocatalysis for Water Purification*, 2015, DOI: 10.1016/C2014-0-02650-0.
2 A. J. Abdul-Zahra, M. S. Mashkour, A. M. Juda and H. A. Al-Sultani, Photocatalytic degradation of paracetamol and procaine, *Int. J. ChemTech Res.*, 2016, **9**, 412–425.
3 S. A. Idrees, S. A. Naman and A. Shorachi, Kinetic and thermodynamic study of Trifluralin photo-degradation by ultra violet light, *IOP Conf. Ser. Mater. Sci. Eng.*, 2018, **454**, 12045.
4 M. M. Molla-Babaker and S. A. Idreesb, Degradation of Congo Red Dye Using Homogeneous Photo Fenton Catalyst Coupled with Oxygen Kinetics and Statistical Analysis, *Asian J. Appl. Chem. Res.*, 2020, **6**, 1–9.
5 V. Loddo, M. Bellardita, G. Camera-Roda, F. Parrino and L. Palmisano, Heterogeneous Photocatalysis: A Promising Advanced Oxidation Process, *Current Trends and Future Developments on (Bio-) Membranes: Photocatalytic Membranes and Photocatalytic Membrane Reactors*, Elsevier Inc., 2018, DOI: 10.1016/B978-0-12-813549-5.00001-3.
6 C. B. Mendive and D. W. Bahnemann, Mechanisms in Heterogeneous Photocatalysis, *Encycl. Mater. Sci. Technol.*, 2011, 1–5, DOI: 10.1016/b978-0-08-043152-9.02273-9.
7 A. R. Khataee and M. Fathinia Recent Advances in Photocatalytic Processes by Nanomaterials, *New and Future Developments in Catalysis: Catalysis by Nanoparticles*, Elsevier B.V., 2013, DOI: 10.1016/B978-0-444-53874-1.00011-1.
8 S. A. Idrees, R. N. Salih, K. Bashir and A. A. Hamasaeed, Kinetic Study of Congo-Red Photo-Catalytic Degradation in Aqueous Media Using Zinc Oxide as Photo Catalyst Under Led Light, *Sci. J. Univ. Zakho*, 2021, **9**, 20–24.
9 M. R. Ashwin Kishore and P. Ravindran, Tailoring the Electronic Band Gap and Band Edge Positions in the C2N Monolayer by P and As Substitution for Photocatalytic Water Splitting, *J. Phys. Chem. C*, 2017, **121**, 22216–22224.
10 K. M. Omer, N. N. Mohammad and S. O. Baban, Up-Conversion Fluorescence of Phosphorous and Nitrogen Co-Doped Carbon Quantum Dots (CDs) Coupled with Weak LED Light Source for Full-Spectrum Driven Photocatalytic Degradation *via* ZnO-CDs Nanocomposites, *Catal. Lett.*, 2018, **148**, 2746–2755.
11 U. J. Ahile, R. A. Wuana, A. U. Itodo, R. Sha'Ato and R. F. Dantas, Stability of iron chelates during photo-Fenton process: The role of pH, hydroxyl radical attack and temperature, *J. Water Process Eng.*, 2020, **36**, 101320.
12 F. Velichkova, Heterogeneous Fenton and Photo-Fenton Oxidation for Paracetamol Removal Using Iron Containing ZSM-5 Zeolite as Catalyst, *AIChE J.*, 2012, **59**, 215–228.
13 F. Audino, et al., A kinetic study for the Fenton and photo-Fenton paracetamol degradation in an annular photoreactor, *Environ. Sci. Pollut. Res.*, 2019, **26**, 4312–4323.
14 S. Hashemian, Fenton-like oxidation of malachite green solutions: Kinetic and thermodynamic study, *J. Chem.*, 2013, **2013**, 809318.
15 J. H. Sun, S. P. Sun, G. L. Wang and L. P. Qiao, Degradation of azo dye Amido black 10B in aqueous solution by Fenton oxidation process, *Dyes Pigm.*, 2007, **74**, 647–652.
16 S. X. Liu, Z. P. Qu, X. W. Han and C. L. Sun, A mechanism for enhanced photocatalytic activity of silver-loaded titanium dioxide, *Catal. Today*, 2004, **93–95**, 877–884.
17 H. Wang, S. Baek, J. Lee and S. Lim, High photocatalytic activity of silver-loaded ZnO-$SnO_2$ coupled catalysts, *Chem. Eng. J. J.*, 2009, **146**, 355–361.
18 S. S. Wong, M. J. Hülsey, H. An and N. Yan, Quantum yield enhancement in the photocatalytic HCOOH decomposition to $H_2$ under periodic illumination, *Catal. Sci. Technol.*, 2022, **12**, 5217–5228.
19 C. B. Mendive, T. Bredow, J. Schneider, M. Blesa and D. Bahnemann, Oxalic acid at the $TiO_2$/water interface under UV(A) illumination: Surface reaction mechanisms, *J. Catal.*, 2015, **322**, 60–72.
20 M. Curti, D. W. Bahnemann and C. B. Mendive, Mechanisms in Heterogeneous Photocatalysis: Titania under UV and Visible Light Illumination, *Ref. Modul. Mater. Sci. Mater. Eng.*, 2016, 1–6, DOI: 10.1016/b978-0-12-803581-8.03800-5.
21 N. Bühler, K. Meier and J. F. Reber, Photochemical hydrogen production with cadmium sulfide suspensions, *J. Phys. Chem.*, 1984, **88**, 3261–3268.
22 X. Ruan, et al., A visible-light-driven Z-scheme CdS/$Bi_{12}GeO_{20}$ heterostructure with enhanced photocatalytic degradation of various organics and the reduction of aqueous Cr(VI), *J. Colloid Interface Sci.*, 2019, **543**, 317–327.
23 M. R. Ashwin Kishore, K. Larsson and P. Ravindran, Two-dimensional CdX/$C_2N$ (X = S, Se) heterostructures as potential photocatalysts for water splitting: A DFT study, *ACS Omega*, 2020, **5**, 23762–23768.
24 B. Zhu, P. Xia, Y. Li, W. Ho and J. Yu, Fabrication and photocatalytic activity enhanced mechanism of direct Z-scheme g-$C_3N_4$/$Ag_2WO_4$ photocatalyst, *Appl. Surf. Sci.*, 2017, **391**, 175–183.
25 T. Chen, et al., Carbon nitride modified hexagonal boron nitride interface as highly efficient blue LED light-driven photocatalyst, *Appl. Catal., B*, 2018, **238**, 410–421.
26 Y. Zhan, et al., Targets regulated formation of boron nitride quantum dots – Gold nanoparticles nanocomposites for ultrasensitive detection of acetylcholinesterase activity and its inhibitors, *Sens. Actuators, B*, 2019, **279**, 61–68.

27 J. H. Jung, et al., Defect engineering route to boron nitride quantum dots and edge-hydroxylated functionalization for bio-imaging, *RSC Adv.*, 2016, **6**, 73939–73946.
28 S. A. Idrees, L. A. Jamil and K. M. Omer, Fabrication Of Novel Metal-Free Phosphorous Doped Boron Nitride As UV. Active Photo-Catalyst, *Iran. J. Catal.*, 2021, **11**, 405–416.
29 Z. He, et al., Formation of heterostructures *via* direct growth CN on h-BN porous nanosheets for metal-free photocatalysis, *Nano Energy*, 2017, **42**, 58–68.
30 J. Yu, et al., Vertically aligned boron nitride nanosheets: Chemical vapor synthesis, ultraviolet light emission, and superhydrophobicity, *ACS Nano*, 2010, **4**, 414–422.
31 D. Huang, M. Cheng, L. Hu and W. Xiong, Semiconductor/boron nitride composites: synthesis, properties, and photocatalysis applications, *Appl. Catal., B*, 2018, **238**, 6–8.
32 S. Angizi, F. Shayeganfar, M. H. Azar and A. Simchi, Surface/edge functionalized boron nitride quantum dots: Spectroscopic fingerprint of bandgap modification by chemical functionalization, *Ceram. Int.*, 2020, **46**, 978–985.
33 B. Liu, et al., One-Step Synthesis of Boron Nitride Quantum Dots: Simple Chemistry Meets Delicate Nanotechnology, *Chem.–Eur. J.*, 2016, **22**, 18899–18907.
34 W. Kohn and L. J. Sham, Self-Consistent Equations Including Exchange and Correlation Effects, *Phys. Rev.*, 1965, **140**, A1133–A1137.
35 C. Lee, W. Yang and R. G. Parr, Development of the Colle-Salvetti correlation-energy formula into a functional of the electron density, *Phys. Rev. B: Condens. Matter Mater. Phys.*, 1988, **37**, 785–789.
36 P. Ju, et al., A novel calcined $Bi_2WO_6/BiVO_4$ heterojunction photocatalyst with highly enhanced photocatalytic activity, *Chem. Eng. J.*, 2014, **236**, 430–437.
37 M. Pirhashemi and A. Habibi-Yangjeh, Ultrasonic-assisted preparation of plasmonic $ZnO/Ag/Ag_2WO_4$ nanocomposites with high visible-light photocatalytic performance for degradation of organic pollutants, *J. Colloid Interface Sci.*, 2016, **491**, 216–229.
38 J. Du, et al., The Research on the Construction and the Photocatalytic Performance of $BiOI/NH_2$-MIL-125(Ti) Composite, *Catalysts*, 2021, **125**, 1–15.
39 F. Cao, et al., An: *In situ* Bi-decorated BiOBr photocatalyst for synchronously treating multiple antibiotics in water, *Nanoscale Adv.*, 2019, **1**, 1124–1129.
40 R. Geick, C. H. Perry and G. Rupprecht, Normal Modes in Hexagonal Boron, *Phys. Rev.*, 1966, **146**, 543–547.
41 B. Singh, G. Kaur, P. Singh, K. Singh and B. Kumar, Nanostructured Boron Nitride With High Water Dispersibility For Boron Neutron Capture Therapy, *Nat. Sci. Rep.*, 2016, **6**, 35535.
42 T. Shen, Highly efficient preparation of hexagonal boron nitride by direct microwave heating for dye removal, *J. Mater. Sci.*, 2019, **54**, 8852–8859.
43 D. G. Ortiz, et al., Exfoliation of Hexagonal Boron Nitride (h-BN) in Liquide Phase by Ion Intercalation To cite this version: HAL Id: hal-01926507 Exfoliation of Hexagonal Boron Nitride (h-BN) in Liquide Phase by Ion Intercalation, *MDPI Nanomater.*, 2018, **8**, 1–12.
44 L. Zhai, et al., Cyanate ester resin based composites with high toughness and thermal conductivity, *RSC Adv.*, 2019, **9**, 5722–5730.
45 D. J. Kester, K. S. Ailey, R. F. Davis, N. Carolina and K. L. More, Phase evolution in boron nitride thin films, *Mater. Res. Soc.*, 1993, **8**, 1213–1216.
46 B. C. Tang, Y. Bando, Y. Huang, C. Zhi and D. Golberg, Synthetic Routes and Formation Mechanisms of Spherical Boron Nitride Nanoparticles, *Adv. Funct. Mater.*, 2008, **18**, 3653–3661.
47 P. M. Sudeep, et al., Functionalized boron nitride porous solids, *RSC Adv.*, 2015, **5**, 93964–93968.
48 X. Luo, Y. Zhang, C. Zandén, M. Murugesan, Y. Cao, L. Ye and J. Liu, Novel thermal interface materials: boron nitride nanofiber and indium composites for electronics heat dissipation applications, *J. Mater. Sci.: Mater. Electron.*, 2014, **25**, 2333–2338.
49 L. Chen, et al., Thermal Conductivity Performance of Polypropylene Composites Filled with Polydopamine-Functionalized Hexagonal Boron Nitride, *PLoS One*, 2017, 1–16, DOI: **10.1371/journal.pone.0170523**.
50 C. Várhelyi, et al., Preparation and characterization of novel $[Fe(methylisopropylglyoximato)_2(amine)_2]$ mixed chelates, *J. Radioanal. Nucl. Chem.*, 2015, **304**, 745–750.
51 L. Nalbandian, et al., Magnetic Nanoparticles in Medical Diagnostic Applications: Synthesis, Characterization and Proteins Conjugation, *Curr. Nanosci.*, 2015, **12**, 455–468.
52 N. R. Jannah and D. Onggo, Synthesis of $Fe_3O_4$ nanoparticles for colour removal of printing ink solution, *J. Phys. Conf. Ser.*, 2019, **1245**, 1–7.
53 A. Azizi, Green Synthesis of $Fe_3O_4$ Nanoparticles and Its Application in Preparation of $Fe_3O_4$/Cellulose Magnetic Nanocomposite: A Suitable Proposal for Drug Delivery Systems, *J. Inorg. Organomet. Polym. Mater.*, 2020, **30**, 3552–3561.
54 E. Bertolucci, et al., Chemical and magnetic properties characterization of magnetic nanoparticles, *Conf. Rec. - IEEE Instrum. Meas. Technol. Conf.*, 2015, 1492–1496.
55 G. C. Fortman, A. M. Z. Slawin and S. P. Nolan, Highly active iridium(III)-NHC system for the catalytic B-N bond activation and subsequent solvolysis of ammonia-borane, *Organometallics*, 2011, **30**, 5487–5492.
56 C. Huang, et al., Stable colloidal boron nitride nanosheet dispersion and its potential application in catalysis, *J. Mater. Chem. A*, 2013, **1**, 12192–12197.
57 V. A. Barinov, V. A. Tsurin, V. I. Voronin, S. I. Novikov and V. T. Surikov, Mössbauer investigations of the metastable Fe23B 6 phase, *Phys. Met. Metallogr.*, 2006, **101**, 456–466.
58 C. I. VillaVelázquez-Mendoza, et al., Effect of substrate roughness, time and temperature on the processing of iron boride coatings: Experimental and statistical approaches, *Int. J. Surf. Sci. Eng.*, 2014, **8**, 71–91.
59 K. H. Jack, The occurrence and the crystal structure of $\alpha'$ ′-iron nitride; a new type of interstitial alloy formed during the tempering of nitrogen-martensite, *Proc. R. Soc. London, Ser. A*, 1951, **208**, 216–224.

60 W. T. Zheng, et al., Crystal structures and magnetic properties of Fe–N thin films deposited by dc magnetron sputtering, *Powder Diffr.*, 2004, **19**, 352–355.
61 L. Pauling and S. B. Hendricks, The crystal structures of hematite and corundum, *J. Am. Chem. Soc.*, 1925, **47**, 781–790.
62 O. O. Kurakevych and V. L. Solozhenko, Rhombohedral boron subnitride, B13N2, by X-ray powder diffraction, *Acta Crystallogr., Sect. C: Cryst. Struct. Commun.*, 2007, **63**, 80–82.
63 A. Brager, An X-ray examination of the structure of boron nitride, *Acta Physicochim.*, 1937, **7**, 699–706.
64 O. Hassel, Die kristalustrakture des boronnitride, BN, *Nor. Geol.*, 1927, **9**, 266–270.
65 H. Türkez, et al., Synthesis, characterization and cytotoxicity of boron nitride nanoparticles: emphasis on toxicogenomics, *Cytotechnology*, 2019, **71**, 351–361.
66 V. Guerra, et al., 2D boron nitride nanosheets (BNNS) prepared by high-pressure homogenisation: Structure and morphology, *Nanoscale*, 2018, **10**, 19469–19477.
67 S. A. Idrees, L. A. Jamil and K. M. Omer, Silver-Loaded Carbon and Phosphorous Co-Doped Boron Nitride Quantum Dots (Ag@CP-BNQDs) for Efficient Organic Waste Removal: Theoretical and Experimental Investigations, *ACS Omega*, 2022, **7**, 37620–37628.
68 Y. Sa, et al., Are different crystallinity-index-calculating methods of hydroxyapatite efficient and consistent?, *New J. Chem.*, 2017, **41**, 5723–5731.
69 Q. Weng, X. Wang, X. Wang, Y. Bando and D. Golberg, Functionalized hexagonal boron nitride nanomaterials: Emerging properties and applications, *Chem. Soc. Rev.*, 2016, **45**, 3989–4012.
70 X. Shi, et al., Few-Layer Hydroxyl-Functionalized Boron Nitride Nanosheets for Nanoscale Thermal Management, *ACS Appl. Nano Mater.*, 2020, **3**, 2310–2321.
71 D. Kim, et al., Sonication-assisted alcoholysis of boron nitride nanotubes for their sidewalls chemical peeling, *Chem. Commun.*, 2015, **51**, 7104–7107.
72 S. Debnath, N. Ballav, H. Nyoni, A. Maity and K. Pillay, Optimization and mechanism elucidation of the catalytic photo-degradation of the dyes Eosin Yellow (EY) and Naphthol blue black (NBB) by a polyaniline-coated titanium dioxide nanocomposite, *Appl. Catal., B*, 2015, **163**, 330–342.
73 S. A. Idrees and M. K. Ibrahim, Optimization of Congo-Red Photo-Catalytic Degradation by Central Composite Design, in *2018 International Conference on Advanced Science and Engineering (ICOASE)*, 2018, pp. 389–393, DOI: **10.1109/ICOASE.2018.8548919**.
74 M. Berkani, Y. Kadmi, M. K. Bouchareb, M. Bouhelassa and A. Bouzaza, Combinatıon of a Box-Behnken design technique with response surface methodology for optimization of the photocatalytic mineralization of C.I. Basic Red 46 dye from aqueous solution, *Arab. J. Chem.*, 2020, **13**, 8338–8346.
75 H. Chaker, N. Ameur, K. Saidi-Bendahou, M. Djennas and S. Fourmentin, Modeling and Box-Behnken design optimization of photocatalytic parameters for efficient removal of dye by lanthanum-doped mesoporous $TiO_2$, *J. Environ. Chem. Eng.*, 2021, **9**, 104584.
76 K. Xie, H. Zhang, S. Sun and Y. Gao, Functions of boric acid in fabricating $TiO_2$ for photocatalytic degradation of organic contaminants and hydrogen evolution, *Mol. Catal.*, 2019, **479**, 110614.
77 S. Ghattavi and A. Nezamzadeh-Ejhieh, A brief study on the boosted photocatalytic activity of AgI/$WO_3$/ZnO in the degradation of methylene blue under visible light irradiation, *Desalin. Water Treat.*, 2019, **166**, 92–104.
78 L. Nadjia, E. Abdelkader and B. Ahmed, Photodegradation study of Congo Red in Aqueous Solution using ZnO/UV-A: Effect of pH And Band Gap of other Semiconductor Groups, *J. Chem. Eng. Process Technol.*, 2011, **02**, 1–7.
79 R. Mohammed, S. Ahmed, A. Abdulrahman and S. Hamad, Synthesis and Characterizations of ZnO Thin Films Grown by Physical Vapor Deposition Technique, *J. Appl. Sci. Technol. Trends*, 2020, **1**, 135–139.
80 A. F. Abdulrahman, S. M. Ahmed and M. A. Almessiere, Effect of the growth time on the optical properties of ZnO nanorods grown by low temperature method, *Dig. J. Nanomater. Biostructures*, 2017, **12**, 1001–1009.
81 A. Habibi-yangjeh and M. Shekofteh-gohari, Novel magnetic $Fe_3O_4$/ZnO/$NiWO_4$ nanocomposites : Enhanced visible-light photocatalytic performance through p–n heterojunctions, *Sep. Purif. Technol.*, 2017, **184**, 334–346.
82 M. Mousavi, A. Habibi-yangjeh and M. Abitorabi, Fabrication of novel magnetically separable nanocomposites using graphitic carbon nitride, silver phosphate and silver chloride and their applications in photocatalytic removal of different pollutants using visibl, *J. Colloid Interface Sci.*, 2016, **480**, 218–231.
83 H. Dong, An advanced Ag-based photocatalyst $Ag_2Ta_4O_{11}$ with outstanding activity, *Phys. Chem. Chem. Phys.*, 2014, 3–6.
84 S. Brook, The absolute energy positions of conduction and valence bands of selected semiconducting minerals, *Am. Mineral.*, 2000, **85**, 543–556.
85 L. Dia, H. Yanga, T. Xian and X. Chen, Enhanced Photocatalytic Degradation Activity of $BiFeO_3$ Microspheres by Decoration with g-$C_3N_4$ Nanoparticles, *Mater. Res.*, 2018, **21**, 5.
86 S. Shenoy and K. Tarafder, Enhanced photocatalytic efficiency of layered CdS/CdSe heterostructures: Insights from first principles electronic structure calculations, *J. Phys. Condens. Matter*, 2020, **32**, 8–14.
87 J. P. Perdew, K. Burke and M. Ernzerhof, Generalized gradient approximation made simple, *Phys. Rev. Lett.*, 1996, **77**, 3865–3868.
88 M. K. Abdel-Sattar and M. Taha, Electronic structures and optoelectronic properties of ATiOPO$_4$ (A = H, Li, Na, K, Rb, Cs, Fr, $NH_4$, Ag) compounds and their applications in water splitting, $CO_2$ reduction, and photo-degradation, *Mater. Res. Express*, 2020, **7**, 045901.
89 M. I. Hussien, et al., Experimental and Theoretical (*ab initio* and DFT) Analysis of UV-Vis Spectra, Thermodynamic Functions and Non-linear Optical Properties of 2-Chloro-

3,4-Dimethoxybenzaldehyde, *J. Adv. Phys.*, 2015, **8**, 1201–1229.

90 T. Rajamani, S. Muthu and M. Karabacak, Electronic absorption, vibrational spectra, nonlinear optical properties, NBO analysis and thermodynamic properties of N-(4-nitro-2-phenoxyphenyl) methanesulfonamide molecule by *ab initio* HF and density functional methods, *Spectrochim. Acta, Part A*, 2013, **108**, 186–196.

91 M. Karabacak, L. Sinha, O. Prasad, Z. Cinar and M. Cinar, The spectroscopic (FT-Raman, FT-IR, UV and NMR), molecular electrostatic potential, polarizability and hyperpolarizability, NBO and HOMO-LUMO analysis of monomeric and dimeric structures of 4-chloro-3,5-dinitrobenzoic acid, *Spectrochim. Acta, Part A*, 2012, **93**, 33–46.

92 H. H. AbdElAziz, M. Taha, W. M. A. El Rouby, M. H. Khedr and L. Saad, Evaluating the performance of $Cs_2PtI_{6-x}Br_x$ for photovoltaic and photocatalytic applications using first-principles study and SCAPS-1D simulation, *Heliyon*, 2022, **8**, e10808.

93 H. Samir, M. Taha, S. I. El-Dek and A. H. Zaki, Electronic Structures and Electrical Properties of $Cr^{2+}$-, $Cu^{2+}$-, $Ni^{2+}$-, and $Zn^{2+}$-Doped Sodium Titanate Nanotubes, *ACS Omega*, 2022, **7**, 27587–27601.

94 H. H. Kora, M. Taha, A. Abdelwahab, A. A. Farghali and S. I. El-Dek, Effect of pressure on the geometric, electronic structure, elastic, and optical properties of the normal spinel $MgFe_2O_4$: A first-principles study, *Mater. Res. Express*, 2020, **7**, 1–11.

95 H. H. Kora, M. Taha, A. A. Farghali and S. I. El-Dek, First-Principles Study of the Geometric and Electronic Structures and Optical Properties of Vacancy Magnesium Ferrite, *Metall. Mater. Trans. A*, 2020, **51**, 5432–5443.

96 M. N. H. Liton, et al., Electronic, mechanical, optical and photocatalytic properties of perovskite $RbSr_2Nb_3O_{10}$ compound, *J. Alloys Compd.*, 2021, **867**, 159077.

97 A. Chakraborty, M. N. H. Liton, M. S. I. Sarker, M. M. Rahman and M. K. R. Khan, A comprehensive DFT evaluation of catalytic and optoelectronic properties of $BaTiO_3$ polymorphs, *Phys. B*, 2023, **648**, 414418.